

LARGE-SCALE PARKER WINDS IN ACTIVE GALACTIC NUCLEI

JOHN E. EVERETT¹ AND NORMAN MURRAY

Canadian Institute for Theoretical Astrophysics, University of Toronto, 60 Saint George Street, Toronto, ON M5S 3H8, Canada

Accepted for publication in the Astrophysical Journal

ABSTRACT

We build and test Parker-wind models to apply to observations of large-scale (~ 100 pc) outflows from Active Galactic Nuclei (AGNs). These models include detailed photoionization simulations, the observed radially varying mass profile, adiabatic cooling, and approximations for clouds dragged along in the wind and the interaction of the wind with the circumnuclear ISM of the galaxy. We test this model against recent *HST*/STIS observations of [O III] emission-line kinematics (in particular, we test against those observed in NGC 4151, but approximately the same kinematics is observed in NGC 1068 and Mrk 3) to constrain the viability of large-scale thermal winds in AGNs. We find that adiabatic cooling dominates in these outflows, decelerating Parker winds on large scales, making them highly unlikely as explanations of the observed kinematics.

Subject headings: galaxies: active — galaxies: Seyfert — galaxies: emission lines — hydrodynamics — radiative transfer — galaxies: individual (NGC 4151, NGC 1068, Mrk 3)

1. INTRODUCTION

Outflows are ubiquitous in astrophysics: they rather paradoxically accompany collapse processes, whether the collapse of a molecular cloud core to form a young stellar object, the collapse of matter onto a galaxy's central black hole, or the collapse of stars into white dwarfs, neutron stars, or black holes. Outflows are important to study for their links to those basic collapse and accretion processes, but also because understanding outflows is crucial to studying the impact and feedback of those winds on the surrounding medium.

Outflows from AGNs are interesting for both of the reasons given above. While there is widespread agreement that AGNs function via accretion from subparsec-scale disks onto super-massive black holes (see, e.g., Peterson 1997; Krolik 1999), the detailed physical processes controlling, for instance, the generation of the continuum, obscuration of AGNs, transferring matter from large (~ 1 kpc) to small scales, as well as the launching mechanisms for outflows, are still not well understood. Most importantly here, while $\sim 50\%$ of AGNs show evidence for outflowing UV and X-ray absorption (Reynolds et al. 1997; George et al. 1998; Crenshaw et al. 1999; Kriss 2001), the physical mechanisms powering those outflows remain unclear. Magnetic fields are a leading candidate for launching winds in both AGNs and young stellar objects (Blandford & Payne 1982; Emmering, Blandford & Shlosman 1992; Contopoulos & Lovelace 1994; Bottorff et al. 1997; Bottorff & Ferland 2000; Bottorff, Korista & Shlosman 2000). In addition, given the high-flux radiation field in some AGNs (especially the high-luminosity quasars), it is also natural and useful to examine radiative acceleration of outflows (McKee & Tarter 1975; Shields 1977; Icke 1977; Shlosman, Vitello & Shaviv 1985; Arav, Li & Begelman 1994; Murray et al. 1995; Chiang & Murray 1996; Proga, Stone & Kallman 2000; Chelouche & Netzer 2001, 2003a,b; Proga & Kallman 2004). Some groups have also combined these two mechanisms, addressing the

importance of radiative acceleration within magnetic winds (Königl & Kartje 1994; de Kool & Begelman 1995; Everett, Königl, & Arav 2002; Everett 2005). Apart from these two models, thermal wind models have also been proposed; several papers have examined X-ray heated winds (Begelman, McKee & Shields 1983; Krolik & Vrtilek 1984; Balsara & Krolik 1993; Krolik & Kriss 1995; Woods et al. 1996; Krolik 1997). Chelouche & Netzer (2005) examined the possibility of thermally-driven (Parker) winds and the ability of those winds to explain observations of low velocity ($v \sim 500$ km s $^{-1}$) X-ray absorption features. In this paper, we also examine the possibility of Parker winds, but in a different context; we test these wind models against spatially resolved observations of the kinematics of forbidden-emission lines (here, [O III]) in local, low-luminosity AGNs.

Forbidden-line emission is very useful for testing models of AGN outflows and their interaction with surrounding gas because such emission is seen at relatively large distances from the nucleus (of order 100 pc). A large distance for the emitting gas is consistent with the observed narrow (low velocity dispersion) emission lines; this region is therefore known as the Narrow Line Region (NLR). The large distance to the NLR is important because whereas many of the physical processes in AGNs occur on scales much too small to directly observe and resolve, the NLR can be and is resolved in some AGNs.

Resolving the NLR is largely a product of the high resolution observations of the *Hubble Space Telescope*, although early ground-based studies of NGC 4151 revealed the possibility of large scale acceleration as early as 1990 (Schulz 1990; Moore, Cohen & Marcy 1996; Moore & Cohen 1996). More recent spectra taken with the *HST*'s Space Telescope Imaging Spectrograph (STIS), however, allow high spatial and spectral resolution studies of the NLR, offering data sufficient to constrain photoionization and dynamical models of the outskirts of AGNs. In particular, Das et al. (2005) have mapped the kinematics of up to three different flux components of [O III] emission in NGC 4151 in five different slits across the observed NLR. In addition, previous studies of the NLR of NGC 4151 (Winge et al. 1999; Nelson et al. 2000; Kraemer et al. 2000) and of the NLR of other AGN (e.g., Crenshaw & Kraemer 2000; Kraemer & Crenshaw 2000; Ruiz et al. 2005) have

Electronic address: everett@physics.wisc.edu, murray@cita.utoronto.ca

¹ Current address: Departments of Astronomy and Physics, and Center for Magnetic Self-Organization in Laboratory and Astrophysical Plasmas, University of Wisconsin, Madison WI 53706 USA

found similar kinematics. The most striking result from these studies is the apparent near-linear increases in velocity ($v \propto r$) over scales from 10 pc to 100 pc and then an apparent linear decrease in velocity at larger scales; further, this trend has been observed on *similar scales in three different objects*: NGC 4151 (Das et al. 2005), NGC 1068 (Crenshaw & Kraemer 2000), and Mrk 3 (Ruiz et al. 2001).

These observations may help constrain the driving forces behind large-scale AGN winds. At first glance, both radiative acceleration and magnetic acceleration are problematic with respect to these observations: both mechanisms accelerate gas to its escape velocity on length scales of order the launching radius. If the outflow is launched from an accretion disk, the launching scale must be $\lesssim 1$ pc (Goodman 2003), and therefore both radiative and magnetic winds would be expected to reach their terminal velocities by approximately 10 pc from the central source. Another possibility for the driving is thermal, or Parker, winds: could such thermal winds accelerate gas slowly enough to explain the observations? This seems plausible, especially if we allow the [O III] emission to originate in clouds dragged along with the wind, which would further slow the observed acceleration. We can then ask what constraints these observations of $v \propto r$ outflows place on thermal wind models. Also, just as important: in the three cases mentioned above, what decelerates the gas? Finally, such models may help constrain the geometry of the NLR (Das et al. 2005).

To address these questions we must build detailed kinematic and photoionization models of the core of AGNs and their winds. In this paper, we build such a thermal wind model (in §2), adapted to considerations of large-scale flows in AGNs, and then apply that model to *HST/STIS* observations of NGC 4151. The particular spectral energy distribution and $M(r)$ profile in NGC 4151 are introduced in §3. The particular mass profile that we adopt allows for a good first-order approximation to the wind as roughly isothermal, so isothermal wind models are applied to NLR observations of NGC 4151 in §4. Isothermality in AGN winds is then tested in the particular case of these thermal winds (and tested against variations in the input spectrum) in §5. We find that thermal wind models face very stringent constraints that make it very unlikely that they can explain the observed NLR kinematics, due chiefly to the effects of adiabatic cooling which ensures that the winds are not isothermal, and in fact cool on large scales ($r \gtrsim 5$ pc).

2. PARKER WINDS

We first review the basic Parker (solar) wind model (§2.1), and then introduce changes to that model that must be included when hypothesizing a large-scale Parker wind at the center of an active galaxy: the increase in enclosed mass as a function of radius, adiabatic cooling for outflows at such large distances, and finally the effects of wind/cloud and wind/ISM drag.

2.1. Parker Winds Applied to AGNs

A Parker wind can be thought of as an extended thermal wind. To explain this terminology, first consider the simplest picture of a thermal wind, where gas at its launch point is heated to high temperature such that that its sound speed is greater than the escape speed ($c_s > v_{\text{escape}}$). This requirement can be recast to ask if the gas temperature is greater than the “escape temperature” $T_g \equiv GM\mu/Rk$ (Begelman, McKee & Shields 1983), where M is the mass of

the central object, μ is the mean mass per particle, R is the launching radius, and k is Boltzmann’s constant. An inherent difficulty with this picture, in relation to the NLR data discussed in the Introduction, is that there is no extended acceleration as is apparently observed.

A Parker wind also depends on thermal effects, but with the major difference that the gas is not heated at the base of the wind to have $c_s > v_{\text{escape}}$. The wind is therefore more like an extended atmosphere, where, at the base of the wind, $c_s \ll v_{\text{escape}}$. The key difference, though, between a Parker wind and an atmosphere is that if such strongly bound gas is heated as a function of height such that the temperature drops more slowly than $M(r)/r$, where $M(r)$ is the enclosed mass and r is the spherical radius, the atmosphere must expand supersonically (explained in more detail later in this section; see Parker 1965). This leads to rather slow acceleration, compared, for instance, to radiatively-driven and magnetically-driven winds.

As mentioned previously, therefore, this model is therefore appealing for the NLR of AGNs. This is especially true of NGC 4151, as photoionization analyses have shown that the central AGN continuum dominates the heating of the NLR (Alexander et al. 1999; Nelson et al. 2000; Kraemer et al. 2000, 2001, and references therein). These photoionization analyses also show that shock heating (which could, for example, result from an interaction with a collimating medium, e.g. Brighenti & Mathews 2006) is also not likely to be important. (We note, though, that Kraemer et al. 2001 find the possibility of shock heating near the start of deceleration of the wind at approximately $r \sim 100$ pc.) It is also possible in some AGNs for the central radio jet to affect the NLR by increasing the NLR line widths (e.g., Nelson & Whittle 1996; Capetti, Macchetto & Lattanzi 1997; Steffen et al. 1997; Axon et al. 1998) but that does not appear to be the case for NGC 4151 (Das et al. 2005).

To examine this possibility in more detail, we start with the basic equation for an isothermal Parker wind:

$$\frac{dv}{dr} = \frac{\frac{2c_s^2}{r} - \frac{GM}{r^2}}{v \left(1 - \frac{c_s^2}{v^2} \right)} \quad (1)$$

where v is the one-dimensional radial velocity, and r is the spherical radius.

Two important insights can be seen from examining Equation 1 closely. First, we note the importance of the “critical point” in this equation. As stated earlier, gas at the base of a Parker wind is gravitationally bound, so that $GM/r^2 \gg c_s^2/r$. Therefore, the numerator of Equation 1 must be negative at the base of the wind; since the denominator is also negative ($v < c_s$), a positive acceleration results. However, as the wind moves outward and v increases, eventually $v = c_s$ and the denominator of Equation 1 becomes zero. In order for the Parker wind equation to be physically meaningful, the numerator must also be equal to zero at the same time the denominator becomes zero, so $2c_s^2/r$ must equal GM/r^2 (or $r = r_{\text{critical}} = GM/2c_s^2$) must be true when $v = c_s$. This requirement sets the location of the critical point: this is the (r, v) pair that the solution must “thread” so that the wind solution can describe a flow that continuously accelerates. In fact, the solution that passes through this critical point is the only solution that allows an outflow to large distances and to speeds above the escape velocity. Physically, this critical point represents the last point downstream in the outflow where the boundary conditions at the disk can communicate with and therefore af-

fect the wind. An example of such a solution is shown by the dashed line in Figure 1, which threads the critical point, indicated by the circle. Other solutions (such as the “breeze” solutions that have $dv/dr = 0$ below the position of the critical point in Fig. 1, achieving smaller peak velocities than the critical point velocity and then decelerating) that do not result in a viable outflow are also shown.

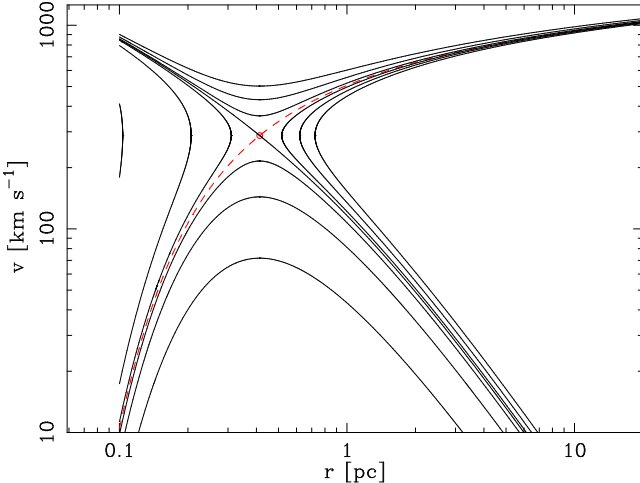


FIG. 1.— A variety of solutions to the Parker wind equation (Eq. 1) for an isothermal wind with $T = 5 \times 10^6$ K, $M_\bullet = 1.3 \times 10^7 M_\odot$, and $r_{\text{launch}} = 0.1$ pc. The dashed line shows the solution that passes from low velocity at the launch point, through the critical point, to high velocity at large distance. This solution, passing through the critical point, is the only steady-state solution that yields a viable wind model. Other solutions, not passing through the critical point, are shown for comparison. For completeness, we also show that it is possible to have an inflow solution that passes through the critical point: gas at high velocity ($v \gg c_s$) at large distance ($r \gg r_{\text{critical}}$) that slows as it falls to the central object; this is known as Bondi-Hoyle accretion (Bondi & Hoyle 1944).

Second, in order to pass through that critical point, there is a further constraint on the temperature structure of the outflow, which was mentioned briefly above. In order for the solution to pass through the critical point and continuously accelerate, the temperature profile, $T(r)$ must decrease with radius less quickly than $M(r)/r$. To show this, we recast the Parker wind equation into a form that shows directly the comparison between the pressure gradient and gravity:

$$v \frac{dv}{dr} \left(1 - \frac{c_s^2}{v^2} \right) = -r^2 \frac{d}{dr} \left(\frac{c_s^2}{r^2} \right) - \frac{GM}{r^2} \quad (2)$$

This equation is simply a more general form (not assuming isothermality) of Equation 1 which will allow us to investigate non-isothermal wind models. The same conditions that applied to the numerator of Equation 1 apply to the right-hand side of Equation 2: namely, it will also have to transition from negative to positive values at the critical point.

Now, instead of assuming an isothermal wind (as in Eq. 1), here we set $T = T(r) = T_0(r/r_0)^\alpha$, but retain the assumption of a central point mass, M . After substituting this into Equation 2 and simplifying, we find:

$$v \frac{dv}{dr} \left(1 - \frac{c_s^2}{v^2} \right) = -\frac{c_{s,0}^2}{r_0^\alpha} (\alpha - 2) r^{\alpha-1} - \frac{GM}{r^2} \quad (3)$$

where $c_{s,0}$ is the sound speed at the base of the wind. One can see that in order for the pressure term to dominate gravity, α

must be greater than -1. To illustrate this, consider the case of $\alpha = -1$ in Equation 3:

$$v \frac{dv}{dr} \left(1 - \frac{c_s^2}{v^2} \right) = \frac{3c_{s,0}^2 r_0}{r^2} - \frac{GM}{r^2} \quad (4)$$

At the base of the wind, the right-hand side of the equation will read $3c_{s,0}^2/r_0 - GM/r_0^2$. Since, at the base of a Parker wind, $c_{s,0}^2 \ll GM/r_0$, this term will be negative at the base of the wind, and since both the pressure gradient term (the first term on the right-hand side) and the gravitational term decrease as r^2 , the right-hand side of the equation will never be positive. In that case, the wind will not accelerate to escape velocity. Therefore, in order for the wind to accelerate in this case (where M is constant with radius), α must be greater than -1. One can derive the same result another way: if $\alpha \leq -1$, the result is a static atmosphere (see Parker 1965).

For large-scale winds ($r \gtrsim 1$ pc) in AGNs, though, $M(r)$ increases with radius. Including the possibility of a spatially-varying $M(r)$ in our requirement on the temperature profile $T(r)$, above, r^α must decrease less quickly than $M(r)/r$ in order to accelerate the wind to large distances. Assuming an isothermal sphere to model the gravitational potential of the circumnuclear matter, we will find that (for NGC 4151) the black hole stops dominating the gravitational potential at approximately 1 pc. Beyond that distance, $M(r) \propto r$. In this regime, assuming a simple $M(r) = M_0(r/r_0)$ for now, Equation 3 becomes:

$$v \frac{dv}{dr} \left(1 - \frac{c_s^2}{v^2} \right) = -\frac{c_{s,0}^2}{r_0^\alpha r} (\alpha - 2) r^\alpha - \frac{GM_0}{r_0 r} \quad (5)$$

Equation 5 then shows that we must have $\alpha > 0$ in order to get large-scale acceleration in a thermal wind. In other words, the wind must have $T(r)$ at least slightly increasing with radius in order for a Parker wind to accelerate.

In order to check this constraint on $T(r)$, we must ensure that we address all of the heating and cooling components in an AGN wind accurately. In §3.1, we will use Cloudy (Version 05.07.06; Ferland et al. 1998) to simulate the photoionization heating, although Cloudy by itself cannot include the effects of adiabatic cooling in the context of our thermal wind and wind geometry (it can calculate adiabatic cooling in the context of its own internal wind models, however). This important cooling source will be considered next.

2.2. Adiabatic Cooling

We will run photoionization simulations at regular positions along the flow, but those separate photoionization simulations will not have any knowledge about the kinematics of the outflow. This would be problematic for these large-scale flows where adiabatic cooling is important (see, e.g. Ruden, Glassgold & Shu 1990; Frank, Noriega-Crespo & Balick 1992; Safier 1993; Shang et al. 2002; Chelouche & Netzer 2005), so we calculate the magnitude of the adiabatic cooling outside of Cloudy and include it as input to Cloudy. The adiabatic cooling is simply calculated from:

$$\frac{dq}{dt} = \frac{d\epsilon}{dt} + P \frac{d}{dt} \left(\frac{1}{\rho} \right) \quad (6)$$

where q is the heat per unit mass, ϵ is the internal energy per unit mass, and $P d(1/\rho)$ is the work per unit mass done by

the expanding gas. After some algebra, the change in internal energy is given by:

$$\rho \frac{d}{dt} \left(\frac{3}{2} \frac{P}{\rho} \right) = \frac{P}{\rho} \frac{d\rho}{dt} \quad (7)$$

Finally, using $\dot{M}_{\text{out}} = 4\pi r^2 \rho v$ to eliminate ρ from the above expression, we find that the adiabatic cooling is given by:

$$\Lambda_{\text{adiabatic}} = \rho c_s^2 \left(\frac{2v}{r} + \frac{a}{v} \right) \text{ ergs cm}^{-3} \text{ s}^{-1} \quad (8)$$

where ρ is the mass density of the outflow, c_s is the speed of sound, v is the radial velocity, r is the distance from the central source, and a is the acceleration in the wind. This particular expression and the above-noted units are those necessary to supply the correct cooling rate to Cloudy; as such, the units on this expression are different from, e.g., Dalgarno & McCray (1972).

For all of the wind solutions found in this work, a/v is at least three orders of magnitude smaller than $2v/r$, so the a/v term is safely neglected.

2.3. Clouds Dragged Via Ram Pressure

We will model the [O III] emission as coming from clouds injected into the wind and accelerated by the ram pressure of the wind on those clouds. The drag force for each individual cloud is computed via (e.g., Smith 1984):

$$F_{\text{drag,cloud}} = \rho_{\text{wind}} (v_{\text{wind}} - v_{\text{cloud}})^2 A_{\text{cloud}} \quad (9)$$

where ρ_{wind} is the mass density of the wind, v_{wind} and v_{cloud} denotes the velocity of the wind and clouds, and A_{cloud} represents the cross sectional area of a cloud. Assuming a spherical cloud with mass $M_{\text{cloud}} = (4/3)\pi r^3 \rho_{\text{cloud}}$, the acceleration for each cloud is

$$a_{\text{drag,cloud}} = \frac{\rho_{\text{wind}} \frac{3}{4} (v_{\text{wind}} - v_{\text{cloud}})^2}{\rho_{\text{cloud}} R_{\text{cloud}}} = \frac{n_{\text{wind}}}{N_{\text{H,cloud}}} \frac{3}{4} (v_{\text{wind}} - v_{\text{cloud}})^2 \quad (10)$$

where R_{cloud} is the radius of an individual cloud. The ratio $n_{\text{wind}}/N_{\text{H,cloud}}$ is a free parameter in our models. We use this parameter for all clouds, although it would be more physically plausible to imagine a range of densities for the clouds intercepting the large-scale thermal wind. This would lead to a range of velocities, which might explain the large ($\sim 500 \text{ km s}^{-1}$) [O III] line widths observed in this object (Das et al. 2005) and seen in many AGNs (Rice et al. 2006). The model presented here solely addresses trends in the observed centroid of the lines, however, and so only a single density ratio is used.

We assume that the drag of the clouds on the wind is negligible compared to the acceleration of the Parker wind.

2.4. Decelerating the Parker wind via ISM drag

The wind is decelerated in much the same way that the clouds are accelerated: ram pressure from the impact on an external medium, which we assume is also broken up into clouds, and is also assumed stationary. Much like before, then, the drag force is given by:

$$a_{\text{drag,ISM clouds}} = \frac{\rho_{\text{wind}}}{\rho_{\text{ISM cloud}}} \frac{\frac{3}{4} v_{\text{wind}}^2}{R_{\text{ISM cloud}}} = \frac{n_{\text{wind}}}{N_{\text{H,ISM cloud}}} \frac{3}{4} v_{\text{wind}}^2 \quad (11)$$

As the wind decelerates, the embedded clouds decelerate as well, as v_{wind} becomes smaller than v_{cloud} in the cloud drag

equation, Eq. 10. Again, $n_{\text{wind}}/N_{\text{H,ISM cloud}}$ is a free parameters in the models we run.

The wind decelerates under this drag force until the wind becomes subsonic, at which point the integration of the equations of motion ceases. However, $v \lesssim c_s$ at such large distances that it does not affect our ability to fit the observed kinematics.

3. APPLYING THE PARKER WIND MODEL TO NGC 4151

The discussion in §2 outlined the basic physics of the Parker wind. Next, the inputs to that model must be defined from the observations of, in this case, NGC 4151. Most importantly for the consideration of heating, the central spectral energy distribution must be realistically modeled (§3.1) and the particular $M(r)$ profile for NGC 4151 must be included (§3.2).

3.1. Modeling the Central Spectral Energy Distribution

An accurate central spectral energy distribution (SED) is very important to understanding the heating and subsequent acceleration of Parker winds in NGC 4151. To model the SED, we use the central continuum of this object as modeled by Kraemer et al. (2000); this continuum is then used as input for the Cloudy photoionization simulations. The continuum has two components: an intrinsic SED and absorption from surrounding gas. The specification for the intrinsic, unabsorbed SED is given in Table 1: the first and last values of α in the table are relatively unimportant, and are specified simply to cut the spectrum off at low and high energies, while the intermediate values of α are from Kraemer et al. (2000). To this simple power law continuum, we add absorption via an X-ray warm absorber and UV absorber (components “X-High” and “DEa” from Kraemer et al. 2000). The “X-High” absorber has a total hydrogen column density of $N_{\text{H}} = 10^{32.5} \text{ cm}^{-2}$ and an ionization parameter of $U = n_{\text{ion}}/n_{\text{H}} = L_{\text{ion}}/4\pi r^2 n_{\text{HC}} = 1.0$ (where L_{ion} is the ionizing luminosity for $E > 13.6 \text{ eV}$), while the “DEa” absorber has a total hydrogen column of $N_{\text{H}} = 10^{19.75} \text{ cm}^{-2}$ with $U = 10^{-3}$ (using the column for the “northeast” absorber from Kraemer et al. 2000); the metallicities listed in Kraemer et al. (2000) are used for these absorption systems and therefore used for all of the photoionization simulations presented here for self-consistency. (The metallicities from Kraemer et al. (2000) includes only those metals with abundances greater than $\sim 10^{-5}$ of hydrogen, and for those metals, differs only by 0.2 dex from Cloudy’s default solar metallicity. Using Cloudy’s default solar metallicity for the remaining calculations results in only insignificant differences in the $T(r)$ calculations in §5.1.) The absolute luminosity was set to $10^{43.56} \text{ erg s}^{-1}$ in the range of 13.6 eV to 1 keV to match the spectrum displayed in Figure 2 of Kraemer et al. (2000). The resultant continuum is then compared to a range of observations in Figure 2. The generally good agreement between the model continuum and the observations is essential for accurately modeling thermal winds in this source.

It is important to note, of course, that the luminosity of NGC 4151 has been observed to vary by factors of a few over the past decade (see, e.g., Kraemer et al. 2005, where the continuum level was seen to be roughly 2.5 times brighter in the 2-10 keV band in 2002 vs. observations in 2000). The continuum that we have assumed here fits reasonably well to the observations of Edelson et al. (1996), taken in December 1993 when NGC 4151 was near its peak historical brightness, so tests with this continuum should yield good estimates for maximum heating of thermal winds. We will also check the dependence of the results on the central continuum in §5.3.

TABLE 1
PARAMETERS FOR NGC 4151'S INTRINSIC, UNABSORBED
SED

E_{begin}	E_{end}	Power Law $\alpha: F_\nu \propto \nu^\alpha$
1.36×10^{-7} eV	1.24×10^{-3} eV	2.5
1.24×10^{-3} eV	13.6 eV	-1.0
13.6 eV	1 keV	-1.4
1 keV	100 keV	-0.5
100 keV	100 MeV	-2.86

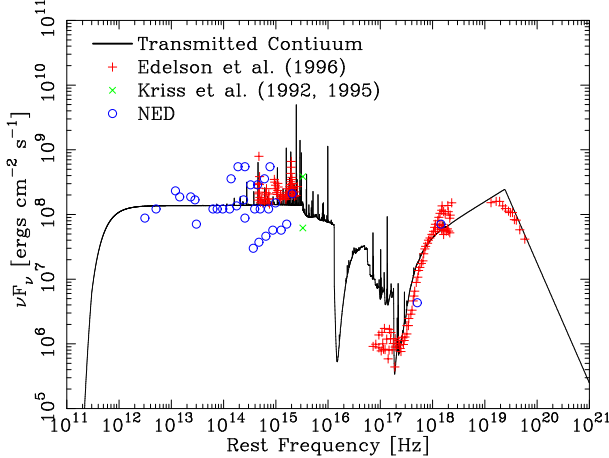


FIG. 2.— Comparison of the assumed central SED for NGC 4151 (defined in Table 1 with added intrinsic absorption) with observations. The solid line shows the SED, modeled by Cloudy, after absorption by components “X-High” and “DEa” from Kraemer et al. (2000). The red data points show the optical, UV, X-ray and γ -ray results from Edelson et al. (1996), the green data points show the range in UV brightness observed during *HUT* pointings (Kriss et al. 1992, 1996), and the blue data points show the wide array of spectral data in NASA’s Extragalactic Database.

We next calculate the Compton temperature for this gas, using the above SED and luminosity to calculate the gas temperature at a range of values for the gas ionization parameter, U . The resultant plot of equilibrium gas temperatures (as in Krolik, McKee & Tarter 1981) is shown Figure 3, which also shows that $T_{\text{e,Compton}} = 3.3 \times 10^7$ K. Note, however, that at extremely high ionization parameters and temperatures ($U/T_{\text{e}} \gtrsim 0.1$; $U \geq 2.5 \times 10^6$ and $T_{\text{e}} \geq 3.3 \times 10^7$ K), the equilibrium temperature starts increasing again. This is due to stimulated Compton heating of the gas, which occurs only at very high ionization parameters: when the radiation field is very intense compared to the gas density (when the electrons are only an “impurity” in the flux of photons), the stochastic electric field of the high-intensity photon field modifies the electrons’ response to the photons, yielding higher heating rates (Levich & Sunyaev 1970; Blandford 1973; Wilson 1982). We include this regime in the equilibrium curves shown here for completeness, but note that even without adiabatic cooling, the ionization parameters in the Parker winds explored here never reach the ionization levels where this extreme heating dominates. In addition, including adiabatic cooling results in significant decreases in this maximum temperature (as already noted, for instance, by Chelouche & Netzer 2005). Given the SED and equilibrium curve, we can ask if the simplest thermal winds could explain the NLR velocities in NGC 4151. For a

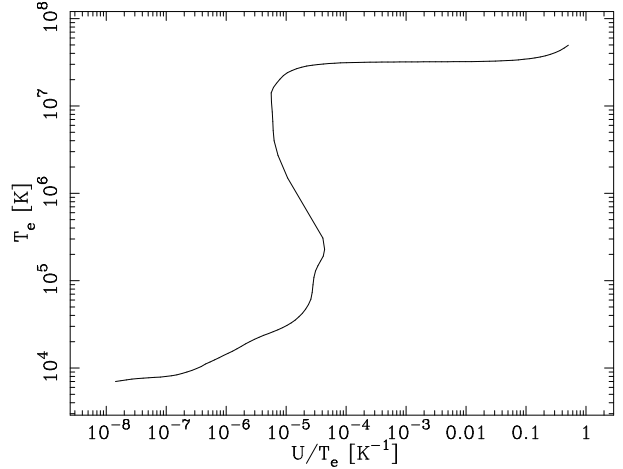


FIG. 3.— The equilibrium “S” curve for the central absorbed SED in Figure 2. This plot shows that the Compton temperature of gas near the central source in NGC 4151 is 3.3×10^7 K. Note the upturn in T_{e} at $U/T_{\text{e}} \gtrsim 0.1$ due to stimulated Compton scattering.

range of initial wind densities, we show the thermal speed and escape speeds for winds launched from 0.1 and 1 parsec in Figure 4. For winds launched at 0.1 pc, the gas is not heated to sufficient temperatures to escape the gravitational potential. Winds launched at $r \gtrsim 1$ pc have sound speeds high enough that gas can be evaporated off the disk and escape the gravitational potential to approximately the correct velocities, although such a simple evaporation model would not explain the large-scale acceleration seen in NGC 4151. However, Figure 4 does show that high density winds will have $c_{s,0} \ll v_{\text{escape}}$, so that Parker winds may be viable solutions (see §2.1).

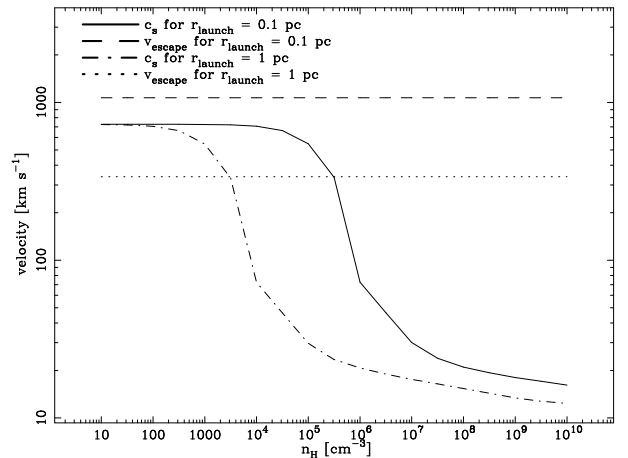


FIG. 4.— The sound speed, c_s , vs n_{H} , the number density, at the disk, using the SED shown in Fig. 2. Only densities for which $c_s > v_{\text{escape}}$ can gas be “evaporated” off of the disk. This figure shows that such evaporation only happens for large distances ($r \gtrsim 1$ pc) and very small densities ($n_{\text{H}} \lesssim 3 \times 10^3$ cm⁻³). This gas is not appreciably accelerated at large distances as is observed, so this model cannot explain the observed velocities in NGC 4151, but it does hint that more detailed thermal winds might be viable models, since approximately the correct velocities can be achieved.

3.2. Radially Increasing $M(r)$

As mentioned in §2.1, the increase in enclosed mass with radius is crucial to modeling thermal winds in AGNs (and has been considered without photoionization simulations by Krolik & Vrtilek 1984). Observationally, the mass distribution within NGC 4151 is not well understood: the only data that exists are estimates of the black hole mass, and estimates of the galaxy's potential at approximately 700 pc. As a first order approximation, we assume an isothermal sphere mass profile and so therefore connect the inferred masses with the following functional form:

$$M(r) = M_{\bullet} + \frac{2r\sigma^2}{G} \quad (12)$$

where $\sigma(r)$ is the observed velocity dispersion at radius r and $M(r)$ is the enclosed mass within radius r .

The central black hole mass is $M_{\bullet} = (1.33 \pm 0.46) \times 10^7 M_{\odot}$ (Peterson 2004). This mass must dominate at small radii (with this $M(r)$ profile, at $r \lesssim 2$ pc). At large radii, the enclosed mass can be derived from HI 21cm line studies; we find the best current constraint to be $\sigma(r = 10'') = 690$ pc $= 122$ km s $^{-1}$ (Mundell et al. 1999). These two data points define our enclosed mass function, $M(r)$.

As discussed in §2.1, $M(r) \propto r$ at large scales in AGN is very important for Parker wind models, as it sets stringent constraints on the $T(r)$ profile required for the Parker wind to be launched to infinity. This $M(r)$ profile also changes the position of the critical point in the wind. Inserting Equation 12 for $M(r)$ into the Parker wind equation (Eq. 1) and solving for the critical point condition, we find

$$r_{\text{critical}} = \frac{GM_{\text{BH}}}{2(c_s^2 - \sigma^2)} \quad (13)$$

In the limit where M_{BH} is dominant ($\sigma = 0$), this equation reduces as expected to the standard expression for the critical point, $r_{\text{critical}} = GM_{\text{BH}}/2c_s^2$. Further, the acceleration at the critical point is also modified from the standard Parker-wind expression because of the inclusion of the $M(r)$ function, and is given by

$$\left(\frac{dv}{dr}\right)_{r=r_{\text{critical}}}^2 = \frac{(c_s^2 - \sigma^2)^3}{(GM_{\text{BH}})^2} \quad (14)$$

These equations allow for integration of the wind equations starting from the critical point.

4. ISOTHERMAL PARKER WIND MODELS

To test the Parker wind model against observations, we first numerically solve the isothermal Parker wind model, integrating from the wind's critical point to the disk and then from the critical point out to where the wind decelerates to $v < c_s$. That 1D solution to the Parker wind is then mapped to a biconical outflow (with geometrical parameters largely similar to those in Das et al.) and then compared to the kinematic data. Our geometry is depicted in Figure 5; the “near” component of the bicone, for NGC 4151, is close to being in the plane of the sky, while the “far” component of the bicone is close to being out of the plane of the sky. We will use this terminology in referring to the different kinematic components of the bicone that are used to explain the spread of observed velocities in our dynamical models.

Given these assumptions about the outflow geometry, the best-fit solution to the data (only for the “north-east” outflow in Slit 1 of the data in Das et al. 2005, as we adopt the geometry from Das et al. and do not fit data from other slits) for

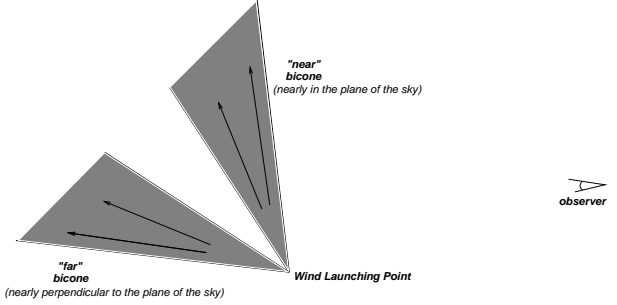


FIG. 5.— A diagram of the biconical geometry for the observed NLR outflow in NGC 4151. The observer, at right, sees the outflow tilted at an inclination angle of 45° to the line of sight. This yields to halves to the bicone with somewhat distinct kinematics: a “near” bicone that is nearly in the plane of the sky, and a “far” bicone with is closer to being perpendicular to the plane of the sky, or nearly along the line of sight of the observer.

the case of clouds being dragged in the wind is shown in Figure 6, where the velocities displayed are the velocities of the embedded clouds as a function of radius along the biconical outflow. This model does a reasonably good job of encompassing the observed velocity data points. For completeness, the thermal wind velocities (the velocities in the continuous wind itself and not the embedded clouds shown in Fig. 6) are displayed in Figure 7. The parameters for this fit as well as “error bars” are given in Table 2. The most important parameter from this table and from the isothermal wind models is the required temperature, $T_e = 3 \times 10^6$ K.

Note that the error bars in Table 2 are only very approximate quantities that result from manually varying each parameter individually, and inspecting a range of fits to the data and picking those fits and ranges of parameter values that seem to best represent the data. We are aware of no method to calculate a χ^2 -like figure-of-merit to quantitatively analyze such data, but present these approximate error bars to communicate the sensitivity of the fit to various parameters. Most importantly, these error bars show that the isothermal wind temperature is fairly well constrained, given the other parameters in the fit. Also, note that the initial radius is very much unconstrained; the only constraint we have here is that $r_0 < 0.8$ pc, which comes from the requirement that $r_0 < r_{\text{crit}}$ for the chosen wind temperature. The geometry of the outflow is also fairly unconstrained in our fits to the data from one slit; assuming that the picture of [O III]-emitting clouds is correct, the inner half-angle of the bicone could be as small as zero, and the outer half-angle of the bicone could be as large as 45°. We have chosen to retain a bicone geometry largely similar to that found in the Das et al. (2005) fits to all of their slits, although the outer bicone half-angle adopted here is 38°, somewhat larger than Das et al.'s estimate of 33° ± 2°. For further comparison to the values in Table 2, Das et al. find a bicone inclination of 45° ± 5°, and an inner bicone half-angle of 15° ± 2°.

Using these best-fit values for the wind, we derive a mass outflow rate in the wind (for the case where $n_0 = 2 \times 10^9$ cm $^{-3}$) of $\dot{M}_{\text{wind}} = 6.6 C_{\text{f,wind}} M_{\odot}$ yr $^{-1}$ where $C_{\text{f,wind}}$ is the global covering fraction of the wind. For the wind parameters found above, $C_{\text{f,wind}} = 0.2$, implying $\dot{M}_{\text{wind}} = 1.3 M_{\odot}$ yr $^{-1}$.

As mentioned previously and as indicated by the organization of Table 2, we can constrain only the ratios $\frac{n_{\text{wind}}}{N_{\text{H,cloud}}}$ and $\frac{n_{\text{wind}}}{N_{\text{H,ISM cloud}}}$. In addition, T and r_{launch} are degenerate as well; a

TABLE 2
INFERRED PARAMETERS FOR THE NLR IN NGC 4151 USING WIND/CLOUD MODEL

Quantity	Value	Range Permissible for Reasonable Fit
Wind Temperature, T	3×10^6 K	$2.5 \times 10^6 - 3.5 \times 10^6$
Launch Radius, r_{launch}	0.1 pc	< 0.8 pc
ISM Gas Radius, r_{ISM}	100 pc	50–150 pc
$\frac{n_{\text{wind}}}{N_{\text{H,ISM}}}$	1.1×10^{-21} cm $^{-1}$	$8.1 \times 10^{-22} - 1.6 \times 10^{-21}$ cm $^{-1}$
$\frac{n_{\text{wind}}}{N_{\text{H,cloud}}}$	6.5×10^{-21} cm $^{-1}$	$2.2 \times 10^{-21} - 3.2 \times 10^{-20}$ cm $^{-1}$
Angle of Inclination of Outflow Cone	45°	
Inner Cone Opening Angle	12°	
Outer Cone Opening Angle	38°	

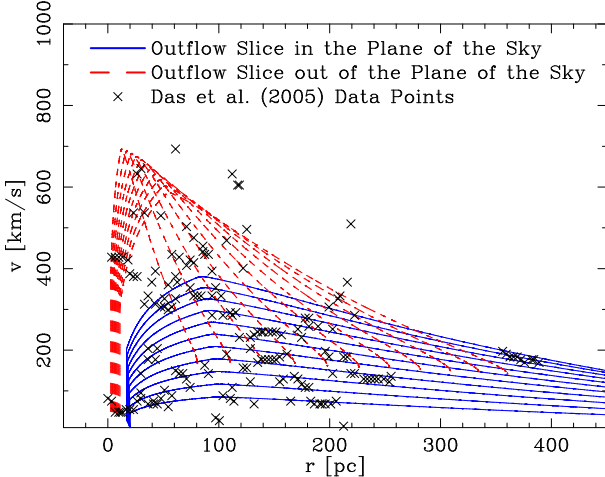


FIG. 6.— The best-fit velocity vs radius profiles for clouds embedded in a biconical, *isothermal* Parker wind (fit parameters are given in Table 2). The blue lines show the velocity results for the clouds on the near side of the outflow, where the outflow bicone is nearly in the plane of the sky, or perpendicular to the line of sight. The red lines give the velocity for the component of the outflow bicone that is close to lying along the line of sight. The range of lines of each color track the velocities for intermediate outflow angles within the assumed bicone. The crosses give the observed velocities for the high-, intermediate-, and lowest-level [O III] flux emission lines from Das et al. (2005).

reasonable fit can be found at larger radii if the temperature drops commensurately.

4.1. The Role of Rotation

We do not include the effects of rotation in this model. Rotation in the Parker Wind would be important very close to the central source, but if angular momentum is conserved in the wind, $v_{\phi,\text{wind}} \sim 4$ km s $^{-1}$ at $r = 20$ pc in this model. This is entirely negligible as the instrument resolution is ~ 40 km s $^{-1}$. The presence of rotation does slightly modify the position of the critical point; we have modified our 1D wind models to include rotation (and verified those models by reproducing, to within 0.1%, the results of Keppens & Goedbloed 1999) and found that rotation modifies the position of the Parker wind's critical point by only 3%; this is relatively insignificant next to the 23% change in the critical point caused by the adoption of the non-point-source gravitational potential. Thus, for these models, we have neglected the effects of rotation.

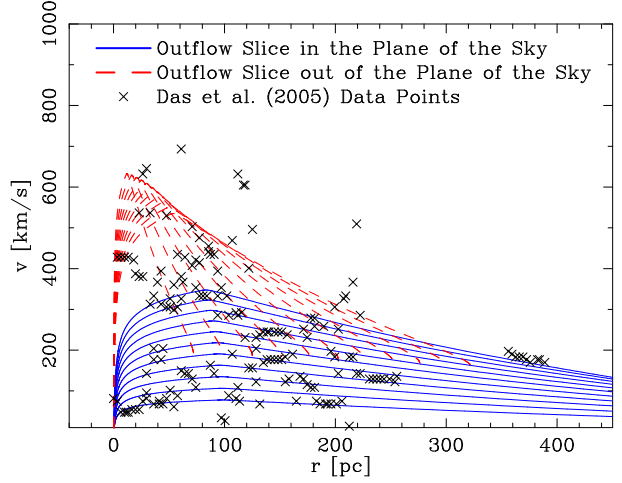


FIG. 7.— As in Fig. 6 but velocities are those for the wind and not the clouds embedded in the wind. (Note the different vertical velocity scale on this plot vs. the velocity scale in Figure 6.)

4.2. The Embedded Clouds: Their Origin, Longevity, and Fate

The clouds in this model are chiefly used to try to slow the apparent acceleration observed in [O III]: our main concern in this paper is to attempt to reproduce the observed kinematics. However, it is interesting to ask about the origin of these clouds, their mass outflow rate, and the various effects of the clouds embedded in the thermal wind.

First, a general overview of the clouds in this model. It is suggested by Das et al. (2005) that STIS can resolve the cloud sizes, so we consider a typical size of a cloud to be $\gtrsim 1$ pc. For the ratio of $n_{\text{wind}}/n_{\text{cloud}}$ found in this model, $\dot{M}_{\text{cloud}} \sim 24.5 C_{\text{f,cloud}} M_{\odot} \text{ yr}^{-1}$ where $C_{\text{f,cloud}}$ is of order 0.1 $C_{\text{f,wind}} \sim 0.02$. This implies a final $\dot{M}_{\text{cloud}} \sim 0.5 M_{\odot} \text{ yr}^{-1}$.

4.2.1. Cloud Origins

Most importantly, in this model, for the parameters that fit this data, clouds cannot be injected into the outflow at the launch point of the wind. The clouds must be injected downstream (the injection in this wind happens at a radius of 20 pc), where the thermal wind's ram pressure is sufficient to override the force of gravity felt by the clouds. If the clouds are injected into or exist in the model at lower radii, those clouds fall back to the base of the wind.

We do not constrain the origin of these clouds any fur-

ther. However, it is reasonable to hypothesis that these clouds (given their size) are portions of large-scale clouds in the inner regions of the galaxy that are entrained in the hot thermal wind. One can also ask if the embedded clouds may form from thermal instabilities in the wind, but our Cloudy models of the wind are stable with the addition of adiabatic cooling (without such cooling, Figs. 3 and 14 show that such a wind at $T \sim 10^6$ K would be thermally unstable, but those figures include only heating by the central continuum and do not include adiabatic cooling). In addition, if clouds were created from thermal instabilities in within the wind, they would share the velocity of the wind; the thermal wind itself accelerates too quickly to explain the slow acceleration of the [O III] clouds, so cloud formation by thermal instability would not explain the observations.

4.2.2. Cloud Emissivity

It is interesting to check whether the emissivity in the clouds is approximately equal to the observed luminosity in [O III]. In addition, is it possible that the clouds, which must be limited in mass in order to be dragged in the wind, cannot have enough mass to account for the [O III] emission?

This is relatively easy to check. Das et al. (2005) report that the [O III] flux from clouds is of order 10^{-12} to 10^{-14} ergs $\text{cm}^{-2} \text{ s}^{-1}$; in particular, near the midpoint of the clouds acceleration at 60 pc, the flux is $\sim 1.6 \times 10^{-14}$ ergs $\text{cm}^{-2} \text{ s}^{-1}$. With NGC 4151 at a distance of ~ 13.3 Mpc, this implies a flux of order $L_{[\text{O III}],\text{observed}} \sim 3 \times 10^{38}$ ergs s. The clouds in this model have a total luminosity of $L_{[\text{O III}],\text{theory}} = 4\pi j_{[\text{O III}]} V$ where $j_{[\text{O III}]}$ is the [O III] line emissivity (in units of $\text{erg s}^{-1} \text{ cm}^{-3} \text{ ster}^{-1}$) and V is the total emission volume. We estimate the volume as $\epsilon^4 \pi r^3$ where ϵ is the cloud volume filling factor, and r_{max} is the outer radius in the wind. To estimate the maximum filling factor for the clouds, we set $\dot{M}_{\text{wind}} v_{\text{wind}} C_{\text{f,wind}} \sim \dot{M}_{\text{wind}} v_{\text{wind}} C_{\text{f,max,clouds}}$ where $C_{\text{f,max,clouds}}$ is the maximum possible cloud covering fraction. For the mass outflow rates inferred in the wind, and the cloud velocities in the wind, we find that $C_{\text{f,max,clouds}} = 0.17$; this is a marginally smaller covering fraction than the wind itself. We then can estimate the cloud volume filling fraction, $\epsilon \lesssim 0.02$. For clouds in the best-fitting wind, we can estimate $j_{[\text{O III}]} \sim 5 \times 10^{-21}$ erg $\text{s}^{-1} \text{ cm}^{-3} \text{ ster}^{-1}$, which implies $L_{[\text{O III}],\text{theory}} \lesssim 6 \times 10^{41}$ ergs s^{-1} . It is somewhat more reasonable to assume that $\epsilon \sim 6 \times 10^{-4}$ (Alexander et al. 1999), which implies $L_{[\text{O III}],\text{theory}} \sim 4 \times 10^{40}$ ergs s^{-1} ; for the simple order-of-magnitude check employed here, this calculation shows that the clouds could indeed account for the observed emissivity, and shows that the cloud filling fraction is reasonably small.

4.2.3. Cloud Longevity

It is also interesting to check the Kelvin-Helmholtz timescales against the acceleration timescales of the clouds to see whether these clouds might be unstable to either Kelvin-Helmholtz or Rayleigh-Taylor instabilities. Both timescales are of order (e.g., Begelman, deKool & Sikora 1991)

$$t_{\text{KH}} \sim \frac{R_{\text{cloud}}}{\delta v} \left(\frac{n_{\text{cloud}}}{n_{\text{wind}}} \right)^{1/2} \sim \left(\frac{R_{\text{cloud}} N_{\text{cloud}}}{n_{\text{wind}}} \right)^{1/2} \frac{1}{\delta v} \quad (15)$$

$$\sim 2.2 \times 10^{19} \text{ s} \left(\frac{R_{\text{cloud}}}{1 \text{ pc}} \right)^{1/2} \frac{1}{\delta v} \quad (16)$$

Meanwhile, the acceleration timescale is of order

$$t_{\text{acc}} \sim \frac{\delta R}{v} \sim 3.1 \times 10^{11} \text{ s} \frac{R_{\text{pc}}}{v_7} \quad (17)$$

where R_{pc} is the acceleration length scale in parsecs, and v_7 is the velocity in units of 10^7 cm s^{-1} . For the parameters of the clouds in our best-fit $n_0 = 2 \times 10^9 \text{ cm}^{-3}$ model, $t_{\text{KH}} > t_{\text{acc}}$ for the clouds out to $r \sim 30$ pc, and t_{KH} is less than t_{acc} by only a factor of less than three, so only large clouds (on scales of 6 pc or more, which would be approximately the size of clouds that Das et al. seem to be resolving in NGC 4151, where $6 \text{ pc} \sim 0.1''$). Our chief concern in this model is in matching the observed dynamics, however.

We can also investigate whether these clouds would be confined by the thermal pressure of the wind. Interestingly, although we did not attempt to satisfy this constraint in our models, the final cloud models are close to being in thermal pressure equilibrium with the thermally-driven wind. We do not model the thermal equilibrium of the clouds, but assuming a cloud temperature of $T_{\text{cloud}} \sim 10^4$ K and a fiducial wind temperature of $T_{\text{wind}} \sim 2 \times 10^6$ K, clouds of radius ~ 0.2 pc would be in approximate thermal equilibrium. Clouds of larger size, such as the clouds apparently required here, would have proportionately smaller densities in our model (in order to reproduce the velocity curves), and so have lower pressures for the assumed T_{cloud} .

We note that it is possible to find a Parker wind solution without clouds that also fits the data, although not as well as the wind and cloud model; note in particular the data points that are not fit near (r, v) values of $(20 \text{ pc}, v \sim 35 \text{ km s}^{-1})$, $(20 \text{ pc}, 400 \text{ km s}^{-1})$, as well as those points above the $r > 100$ pc velocity envelope of the wind. This solution is displayed in Figure 8, with parameters listed in Table 3; note that we fit the wind-only model using the same geometry as used in the wind+cloud model. Since this wind-only model simultaneously results in a somewhat worse fit and similar parameters for the previous model, we consider the previous wind and cloud model the best representation of the data.

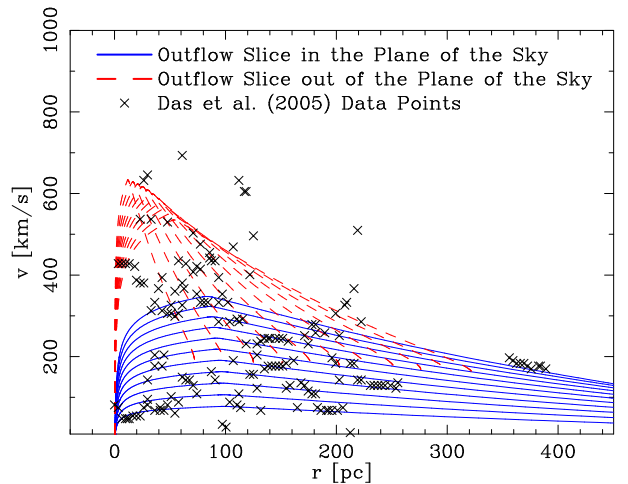


FIG. 8.— The velocity vs distance profiles of the biconical outflow for the best fit model for the wind alone, without any embedded clouds. The data points are the same as those in Figures 6 and 7.

5. TESTS OF PHOTOIONIZATION CONSISTENCY: CAN AN ISOTHERMAL WIND EXIST IN NGC 4151?

TABLE 3
INFERRED PARAMETERS FOR THE NLR IN NGC 4151 USING WIND MODEL

Quantity	Value	Range Permissible for Reasonable Fit
Wind Temperature, T	2.2×10^6 K	$2.0 \times 10^6 - 2.4 \times 10^6$
Launch Radius, r_{launch}	0.1 pc	< 0.8 pc
ISM Gas Radius, r_{ISM}	100 pc	50–210 pc
$\frac{n_{\text{wind}}}{n_{\text{H,ISM}}$ cloud}	1.1×10^{-21} cm $^{-1}$	$7.4 \times 10^{-22} - 1.4 \times 10^{-21}$ cm $^{-1}$
Angle of Inclination of Outflow Cone	45°	
Inner Cone Opening Angle	12°	
Outer Cone Opening Angle	38°	

Having defined an optimum temperature to fit the observations (see Table 2), we now test whether the temperatures required in the isothermal models can be achieved via photoionization from the central AGN. We also check for how the temperature varies as a function of radius in the wind, to test if the wind does indeed have $T(r)$ decreasing less quickly than $1/r$ on small scales and $T(r)$ at least constant on large scales, as required by the Parker wind model (see §2.1). Note that for the initial photoionization tests we present, the run of density vs. radius from the isothermal Parker-wind model is used to set the density at each radius in the wind, so these models are not completely self-consistent. We will then conclude by testing an “X-ray rich” continuum to see if this can help explain the observations, and then finally we will test a non-isothermal Parker wind (with a photoionization-derived $T(r)$ profile) against the observations.

5.1. Photoionization Results

In order to look for a physically consistent thermal wind model that matches the earlier isothermal model and the observations, we ask (1) whether a roughly isothermal temperature structure can be achieved in an AGN wind, (2) whether the temperature is high enough to roughly match the temperature required in the isothermal wind model, and (3) whether $T(r)$ decreases less quickly than $M(r)/r$.

To answer the first two questions, we calculate the temperature as a function of radius for winds with a range of initial densities, $n_{\text{H},0}$, displayed in Figure 9. The temperature vs. radius for each $n_{\text{H},0}$ is calculated by taking the $n(r)$ profile from the isothermal wind model and running Cloudy photoionization simulations at a range of radii given the central continuum of NGC 4151 (defined in §3.1). This figure shows that only for very large $n_{\text{H},0}$ is the wind approximately isothermal. The only initial density in Figure 9 that leads to an approximately isothermal wind is $n_{\text{H},0} = 3.3 \times 10^{10}$ cm $^{-3}$. This density is so high that the resultant wind temperatures rise only to $T_{\text{e,max}} \sim 10^5$ K. Such a temperature is far too low to explain the observed velocities in NGC 4151 which required $T_{\text{e}} = 3 \times 10^6$ K. Lower densities ($n_{\text{H},0} \lesssim 3.3 \times 10^9$) are also not possible in this model as $T(r)$ always drops significantly at large distances. This is simply due to adiabatic cooling. With adiabatic cooling switched off, the temperature in the wind very quickly achieves $T_{\text{e}} \approx 3 \times 10^7$ K and remains at that constant temperature over the rest of the outflow. Even with adiabatic cooling included, however, Figure 9 also shows that $n_{\text{H},0} \sim 2 \times 10^9$ cm $^{-3}$ can achieve approximately the required temperatures over at least a limited range of radii in the outflow; the drop in $T(r)$ at larger distances shows that it may still be problematic, however.

Next, we focus on how quickly the temperature can change with radius and still allow a Parker wind to form. Figure 10 displays the exponent of a piecewise power law that fits the temperature profile shown in Figure 9. Again, in order for a physically consistent Parker wind to exist in the core of NGC 4151, $T(r)$ must drop less slowly than $1/r$ for small distances ($r \lesssim 2$ pc), and then, where $M(r)$ increases almost linearly with radius, $T(r)$ must be, at least, approximately constant: it must have a power law index > 0 . This is true for the high density run with $n_{\text{H},0} = 3.3 \times 10^{10}$ cm $^{-3}$, but as already shown in Figure 9, that wind does not have temperatures high enough to yield the observed velocities. The lower density trials meanwhile show extraordinarily large changes in T_{e} with radius. For $n \leq 3.3 \times 10^8$ cm $^{-3}$, $T(r)$ drops below a power law index value of zero at $r < 0.7$ pc. In contrast, acceleration of the *isothermal* Parker wind must continue out to a few times the Parker wind’s critical point distance, which is at $r_{\text{crit}} \sim 1$ pc for the isothermal wind model shown in Figure 6 (non-isothermal wind models have critical points even further out, since much of the wind’s acceleration occurs with $T(r) < T_{\text{isothermal}}$). However, the temperature is already dropping precipitously at radii even smaller than r_{crit} for $n_{\text{H},0} \leq 3.3 \times 10^8$ cm $^{-3}$, so that range of densities would not yield a Parker wind.

The test case of $n_{\text{H},0} = 2 \times 10^9$ cm $^{-3}$ is closer to having the required temperature (at least at its maximum temperature), and is closer to the desired $T(r)$ profile, and so more careful consideration is justified in this case. As shown in Figure 9, this model does, if only in a limited range of radii, achieve approximately the temperature of the best-fitting isothermal model. Figure 10 shows that the temperature does not drop appreciably until $r \sim 2$ pc. We would expect that since acceleration in the wind is required out to a few parsecs, this temperature profile would also not lead to a viable Parker wind model. But, as the temperature profile is close to satisfying the requirements on $T(r)$, we build a numerical Parker wind model for generic $T(r)$ from our photoionization simulations that finds, self-consistently, the critical point for that particular temperature law. Applying this model to $T(r)$ for the case of $n_{\text{H},0} = 2 \times 10^9$ cm $^{-3}$, we found that the wind decelerates beyond $r = 8$ pc, and so would not fit the required $v(r)$ profile. Testing to see if this $n_{\text{H},0} = 2 \times 10^9$ cm $^{-3}$ profile results in clouds velocities that might fit the data, we apply the same geometry and drag parameters as used in the previous best-fit model (see Table 2) and present the model vs. the data from Das et al. (2005) in Figure 11. The model clearly cannot fit the observed velocities, or their variation with distance.

If we instead use the $T(r)$ profile derived from the $n_{\text{H},0} = 3.3 \times 10^8$ cm $^{-3}$ wind model, we again find a wind that deceler-

ates too quickly (here, the wind starts decelerating at $r = 4$ pc). Attempting to fit this model to the data from Das et al. (2005) results in a much better fit (see Figure 12) than in Figure 11, but still misses the high velocity data points shown in the figure. Modifying the drag term in our wind equation does not improve the fit: decreasing the drag term to fit the higher-velocity points simply increases the outflow velocities, therefore doing an increasingly worse job of fitting the data points near $(r, v) = (70$ pc, 350 km s $^{-1}$). Also, modifying the geometry of the outflow has no significant impact on the fit: the half-angle of the bicone is already 38° here; increasing that to a maximum value of 45° helps to include some of the higher velocity data points, but cannot make up for the discrepancy relative to the isothermal model. Still, this model represents the closest fit to the data achievable with a more realistic $T(r)$ profile; there is no quantitative way to distinguish this fit from the previous isothermal best-fit, but it is perhaps encouraging; this model will be examined in more detail in §5.2. Unfortunately, all of the rest of the generic $T(r)$ models cannot come close to reproducing the data (as can be seen, for example, in Fig. 11).

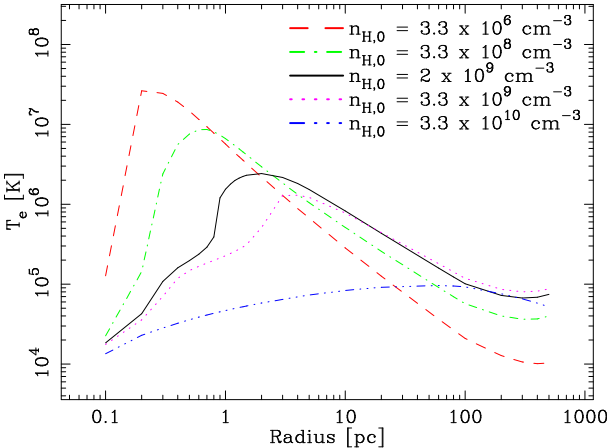


FIG. 9.— T_e in the wind as a function of radius in the Parker wind. As shown in the figure, both the rise in T_e as a function of radius and the maximum T_e achieved are strongly dependent on the initial density. Only winds with $n_{H,0} \lesssim 2 \times 10^9$ cm $^{-3}$ achieve temperatures of $T \sim 3 \times 10^6$ K required by the isothermal Parker wind model. Note also the slower increase of T_e with radius as the density increases.

5.2. How does a self-consistent $T(r)$ affect the Parker wind simulations?

Up until this point, we have used the $n(r)$ profile from an isothermal Parker wind model as input to a set of photoionization models, only rescaling the base density to test different initial densities. It is important to check if the fitting results improve with a more self-consistent $T(r)$, $n(r)$, and $v(r)$ profile instead of using the isothermally-derived $n(r)$ profile to calculate $T(r)$, as before.

We test this possibility by examining the $T(r)$ profile from the $n_0 = 3.3 \times 10^8$ cm 3 simulation (shown in Fig. 9). This is then input into our non-isothermal Parker wind model, and the resulting acceleration profile and $n(r)$ profile is computed. This $n(r)$ profile is then used as the basis for another iteration of Cloudy simulations, to compute the resultant $T(r)$. We ask whether the result of this iteration on the $T(r)$ structure will result in a temperature profile more suitable for a large-scale Parker wind. However, the resulting $T(r)$ profile only

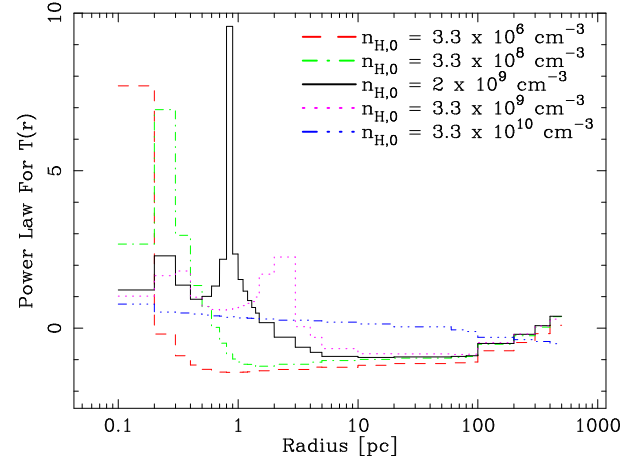


FIG. 10.— A piecewise power-law fit to the temperature data in Figure 9, with the power law, α defined via $T \propto r^\alpha$ for radii between the photoionization simulation results. Physically consistent Parker winds in the NLR of NGC 4151 would require $T(r)$ dropping less quickly than $1/r$ out to $r \sim 2$ pc, and $T(r)$ at least constant out to $r \sim 10$ pc in order for the wind to accelerate. As can be seen here, this is very difficult for any of the winds (given the dominance of adiabatic cooling at large radii) to satisfy.

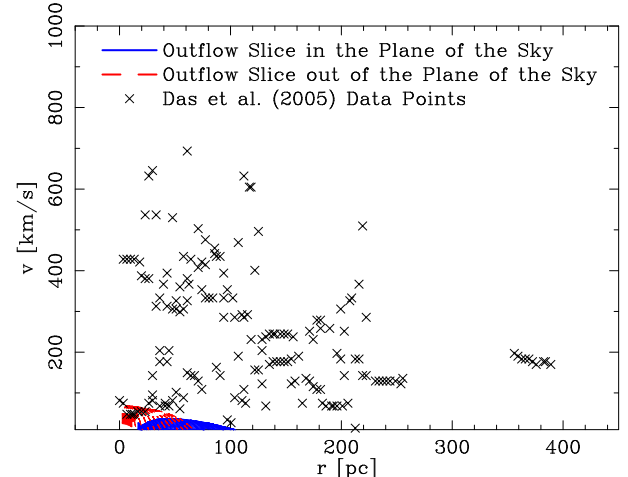


FIG. 11.— As in Figure 6, but with a Cloudy-derived $T(r)$ profile for $n_{H,0} = 2 \times 10^9$ cm $^{-3}$. The wind, with a maximum velocity of only ~ 365 km s $^{-1}$ (the cloud velocities, shown here, do not even approach that velocity), and decelerating for $r > 8$ pc, cannot drag the clouds to anywhere near the observed velocities.

results in a worse fit to the data: the rise in the initial $T(r)$ profile at $r < 1$ pc causes the wind model to accelerate from the disk faster than the fiducial isothermal wind model. This increase in acceleration yields a wind that must be launched from larger radii ($r \sim 0.2$ pc instead of 0.1 pc) and also has a faster dropoff in density with height, which then yields a $T(r)$ curve closer to the lower-density curves in Figure 9: the self-consistent $T(r)$ only results in a less isothermal wind model whose temperature decreases more quickly with radius beyond $r \approx 1$ pc. Therefore, attempting to include a self-consistent temperature profile in the Parker wind model only results in a more rapidly increasing (and then more rapidly decreasing) $T(r)$ profile, which results in a wind model that has a $T(r)$ profile even less suited for accelerating a wind that might fit the observations of Das et al. (2005). So, in the end,

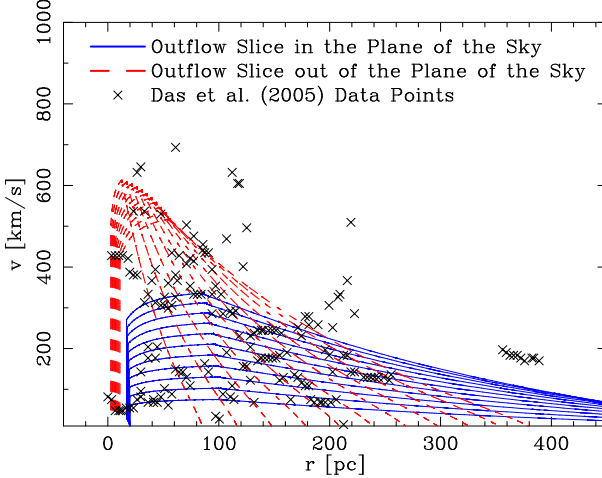


FIG. 12.— As in Figure 6, but with a Cloudy-derived $T(r)$ profile for $n_{H,0} = 3.3 \times 10^8 \text{ cm}^{-3}$.

including such a $T(r)$ profile in the Parker wind also cannot explain the observed acceleration in NGC 4151.

5.3. Does an X-ray “rich” continuum help?

To test the limits of our model of the central continuum, we now adopt a relatively X-ray-bright continuum to check if such a continuum would heat the gas to higher temperatures and modify our results. Displayed in Figure 13, this continuum was primarily modified in the high-energy X-ray regime to more closely follow the observations of Edelson et al. (1996) and the inferred high-energy spectrum of Alexander et al. (1999); we continue to include the UV absorption, as before. This increase in X-ray brightness increases Compton heating within the gas. Meanwhile, the low-energy continuum in the SED has been significantly cut off below 1 eV in order to reduce Compton cooling by low-energy photons as much as possible. This was done, for instance, in Krolik (1999) to account for the possibility that lower-energy photons are emitted at much larger scales and so might not act to cool the outflow in the immediate vicinity of the central black hole. (In reality, for the large-scale winds tested here, the question of the origin of the low-energy photons is less important since they almost certainly play a role on scales of 10 pc. However, to test the limits of the input continuum model, we attempt such a continuum anyway.)

Adopting this continuum does not greatly modify the Compton temperature of the gas. The radiative equilibrium curve for this continuum is shown in Figure 14; for this continuum, $T_{\text{Compton}} = 4.2 \times 10^7 \text{ K}$ as opposed to $T_{\text{Compton}} = 3 \times 10^7 \text{ K}$ for the original continuum.

As one might infer from that relatively small change in the Compton temperature of the gas, adopting this continuum for calculating $T(r)$ does not result in significant changes to our results. We also calculated a self-consistent Parker wind after inputting this continuum into our photoionization simulations, which yielded no appreciable difference from the tests with the original SED. Overall, adopting this SED does not significantly alter any of our conclusions. An X-ray “rich” continuum for the central SED of NGC 4151 cannot help a Parker wind model to explain the observed velocity trends.

6. CONCLUSIONS

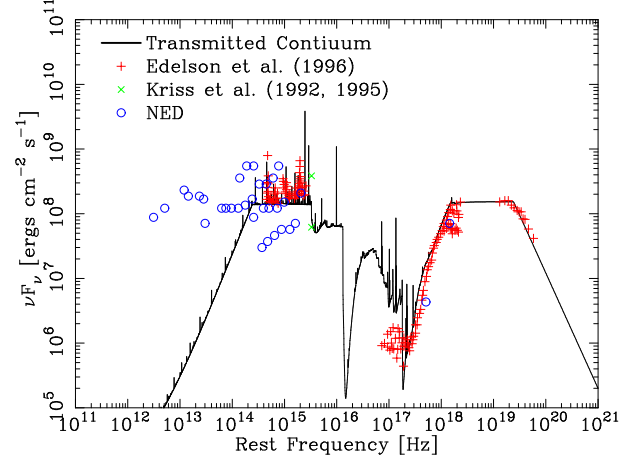


FIG. 13.— An alternate X-ray “rich” incident continuum for NGC 4151, plotted with the same data as in Fig. 2. For this continuum, we explicitly set the high-energy X-ray continuum to fit Edelson et al. (1996), as opposed to the previously adopted continuum, which adopted the Kraemer et al. (2000) power law in the X-rays. This led to slightly higher X-ray flux. At the same time, the continuum below 1 eV was suppressed to lower Compton cooling in the outflow (as in Krolik 1999).

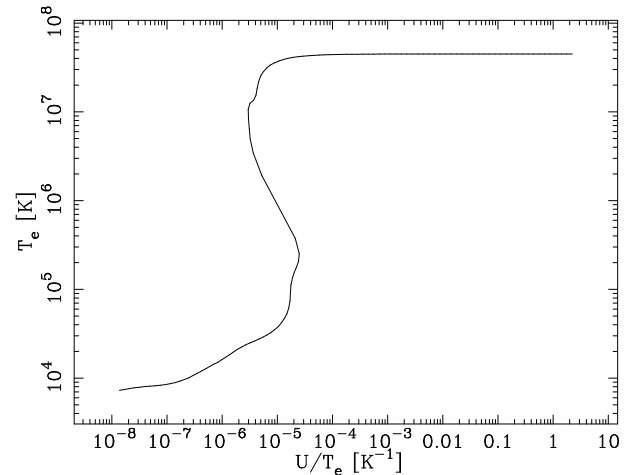


FIG. 14.— The photoionization equilibrium curve for the SED shown in Fig. 13. As can be seen by comparing to Fig. 3, T_{Compton} does not change appreciably.

We have developed models of Parker winds accounting for the effects of the radially varying $M(r)$, adiabatic cooling, and drag effects between the wind and embedded clouds as well as drag forces between the wind and an external medium. We then tested these models against the conditions that exist in the center of one particular local AGN, NGC 4151. We have shown that simple thermal winds cannot explain the slow acceleration that has been inferred for the NLR of NGC 4151. The strongest constraint against self-consistent Parker winds is that adiabatic cooling on the large scales of these outflows leads to temperatures in the wind that decreases strongly as a function of r . With such a temperature profile, Parker winds cannot be launched and accelerated to the observed velocities at the observed distances. Varying the initial density in the wind either yields temperatures that drop quickly with distance (for $n_{H,0} \lesssim 10^8 \text{ cm}^{-3}$) or temperatures that are too low to reproduce the observed velocities ($n_{H,0} \gtrsim 10^9 \text{ cm}^{-3}$). The

intermediate case of $n_{\text{H},0} \sim 3 \times 10^8 \text{ cm}^{-3}$ comes closest to reproducing the data, yielding a temperature profile that we have checked by developing a numerical Parker wind model for general $T(r)$. For the temperature profile shown in Figure 9, the wind starts decelerating already at $r \sim 4 \text{ pc}$; a radius much smaller than the 100 pc out to which acceleration is inferred in NGC 4151. We find that plotting the resultant predicted $v(r)$ against the data from Das et al. (2005) shows that this wind model cannot reproduce the range of [O III] velocity points (see Fig. 12) as well as the isothermal wind model (which cannot be obtained for NGC 4151). Further, attempting to develop a self-consistent $T(r)$ profile for this wind results in a temperature profile even further from isothermal which correspondingly fails to fit the data. In short, we find no self-consistent $T(r)$ profile for a large-scale Parker wind that can explain the observed ranges of velocities.

If thermal winds are not driving the observed $v(r)$ profile, how can it be explained? Radiative driving is most likely not the source of the acceleration: we have tested simple models of radiative acceleration on dust, and such models achieve terminal velocities at distances of order the launch radius – much closer to the launch point than the observed velocity profiles. Magnetic winds would also achieve their terminal velocities on similar scales (although perhaps clouds dragged in the magnetic wind might yield the slow acceleration seen).

The difficulty in fitting this data with almost any known wind model leads us to question whether the observed velocity law is actually a wind accelerating with radius. Perhaps the observed kinematic profile is the result of an interaction of a wind with the surrounding medium. An interesting alternative interpretation is suggested in the work of Matzner & McKee

(1999), which showed that rather generic hydromagnetic winds, expanding into gas surrounding a young stellar object at the wind's terminal velocity, would yield $v \propto r$, or a “Hubble law”-type flow. This is a promising theory for the accelerating portion of the outflow, but it seems unclear how the observed slow deceleration of the flow in NGC 4151 could then be explained in the same picture. Still, it is important to point out that given the inability of a wide range of wind models to explain the observed $v(r)$ profile, perhaps these observations are not revealing acceleration of a wind, but instead the interaction of an already accelerated wind with the surrounding medium.

7. ACKNOWLEDGMENTS

The authors wish to thank Mike Crenshaw, Alvin Das, Steve Kraemer and Chris Matzner for helpful conversations while this work was in progress. We also thank our referee for a helpful and insightful report. Many thanks to Gary Ferland and his collaborators for the development, distribution, and support of Cloudy, which was used in this work. This research was supported by the Natural Sciences and Engineering Research Council of Canada. JEE was also supported by NSF AST-0507367 and NSF PHY-0215581 (to the Center for Magnetic Self-Organization in Laboratory and Astrophysical Plasmas). This research has made use of the NASA/IPAC Extragalactic Database (NED) which is operated by the Jet Propulsion Laboratory, California Institute of Technology, under contract with the National Aeronautics and Space Administration. This research has made use of NASA's Astrophysics Data System.

REFERENCES

Alexander, T., Sturm, E., Lutz, D., Sternberg, A., Netzer, H. & Genzel, R. 1999, *ApJ*, 512, 204

Arav, N., Li, Z.-Y., Begelman, M. 1994, *ApJ*, 432, 62

Axon, D.J., Marconi, A., Capetti, A., Machetto, F.D., Schreier, E. & Robinson, A. 1998, *ApJ*, 496, 75

Balsara, D.S. & Krolik, J.H. 1993, *ApJ*, 402, 109

Begelman, M.C., de Kool, M. & Sikora, M. 1991, *ApJ*, 382, 416

Begelman, M.C., McKee, C.F., Shields, G.A. 1983, *ApJ*, 271, 70

Blandford, R.D. 1973, *A&A*, 26, 161

Blandford, R.D. & Payne, D.G. 1982, *MNRAS*, 199, 883

Bondi, H. & Hoyle, F. 1944, *MNRAS*, 104, 273

Bottorff, M., Korista, K.T., Shlosman, I., Blandford, R.D. 1997, *ApJ*, 479, 200

Bottorff, M.C. & Ferland, G.J. 2000, *MNRAS*, 316, 103

Bottorff, M.C., Korista, K.T. & Shlosman, I. 2000, *ApJ*, 537, 134

Brightenti, F. & Mathews, W.G. 2006, *ApJ*, 643, 120

Capetti, A., Macchetto, F.D., Lattanzi, M.G. 1997, *ApJ*, 476, L67

Chelouche, D. & Netzer, H. 2001, *MNRAS*, 326, 916

Chelouche, D. & Netzer, H. 2003, *MNRAS*, 344, 223

Chelouche, D. & Netzer, H. 2003, *MNRAS*, 344, 233

Chelouche, D. & Netzer, H. 2005, *ApJ*, 625, 95

Chiang, J. & Murray, N. 1996, *ApJ*, 466, 704

Contopoulos, J. & Lovelace, R.V.E. 1994, *ApJ*, 429, 139

Crenshaw, D.M., Kraemer, S.B., Boggess, A., Maran, S.P., Mushotzky, R.F., & Wu, C.-C. 1999, *ApJ*, 516, 750

Crenshaw, D.M. & Kraemer, S.B., 2000, *ApJ*, 532, L101

Dalgarno, A. & McCray, R.A. 1972, *ARA&A*, 10, 375

Das, V., et al. 2005, *AJ*, 130, 945

Edelson, R.A. et al. 1996, *ApJ*, 470, 364

Emmering, R.T., Blandford, R.D. & Shlosman, I. 1992, *ApJ*, 385, 460

Everett, J.E., Königl, A. & Arav, N. 2002, *ApJ*, 569, 671

Everett, J.E. 2005, *ApJ*, 631, 689

Ferland, G.J., Korista, K.T., Verner, D.A., Ferguson, J.W., Kingdon, J.B., Verner, & E.M. 1998, *PASP*, 110, 761

Frank, A., Noriega-Crespo, A. & Balick, B. 1992, *AJ*, 104, 841

George, I.M., Turner, T.J., Netzer, H., Nandra, K., Mushotzky, R.F. & Yaqoob, T. 1998, *ApJS*, 114, 73

Goodman, J. 2003, *MNRAS*, 339, 937

Ikke, V. 1977, *Nature*, 266, 699

Keppens, R. & Goedbloed, J.P. 1999, *A&A*, 343, 251

Königl, A. & Kartje, J.F. 1994, *ApJ*, 434, 446

de Kool, M. & Begelman, M.C. 1995, *ApJ*, 455, 448

Kraemer, S.B. & Crenshaw, D.M. 2000, *ApJ*, 544, 763

Kraemer, S.B., Crenshaw, D.M., Hutchings, J.B., Gull, T.R., Kaiser, M.E., Nelson, C.H., & Weistropp, D. 2000, *ApJ*, 531, 278

Kraemer, S.B., et al., 2001, *ApJ*, 551, 671

Kraemer, S.B., et al., 2005, *ApJ*, 633, 693

Kriss, G.A. et al. 1992, *ApJ*, 392, 485

Kriss, G.A., Davidsen, A.F., Zheng, W., Kruk, J.W. & Espey, B.R. 1995, *ApJ*, 454, L7

Kriss, G.A. 2001, in *Mass Outflow in Active Galactic Nuclei: New Perspectives*, Eds. D.M. Crenshaw, S.B. Kraemer & I.M. George (ASP: San Francisco), 255, 69

Krolik, J.H. 1997, *Ap&SS*, 248, 207

Krolik, J.H. 1999, *Active Galactic Nuclei: From the Central Black Hole to the Galactic Environment* (Princeton: Princeton University Press)

Krolik, J.H. & Kriss, G.A. 1995, *ApJ*, 447, 512

Krolik, J.H., McKee, C.F. & Tarter, C.B. 1981, *ApJ*, 249, 422

Krolik, J.H. & Vrtilek, J.M. 1984, *ApJ*, 279, 521

Levich, E.V. & Sunyaev, R.A. 1970, *Astroph. Lett.*, 7, 69

Matzner, C.D. & McKee, C.F. 1999, *ApJ*, 526, L109

McKee, C.F. & Tarter, C.B. 1975, *ApJ*, 202, 306

Moore, D., Cohen, R.D., Marcy, G.W. 1996, *ApJ*, 470, 280

Moore, D. & Cohen, R.D. 1996, *ApJ*, 470, 301

Mundell, C.G., Pedlar, A., Shone, D.L. & Robinson, A. 1999, *MNRAS*, 304, 481

Murray, N., Chiang, J., Grossman, S.A., Voit, G.M. 1995, *ApJ*, 451, 498

Nelson, C.H. & Whittle, M. 1996, *ApJ*, 465, 96

Nelson, C.H. et al. 2000, *ApJ*, 531, 257

Parker, E.N. 1965, *SSRV*, 4, 666

Peterson, B.M. 1997, *An Introduction to Active Galactic Nuclei* (New York:Cambridge University Press)

Peterson, B.M., et al. 2004, *ApJ*, 613, 682

Proga, D. & Kallman, T.R. 2004, *ApJ*, 616, 688

Proga, D., Stone, J.M. & Kallman, T.R., *ApJ*, 543, 686

Reynolds, C.S. 1997, *MNRAS*, 286, 513

Rice, M.S., Martini, P., Greene, J.F., Pogge, R.W., Shields, J.C., Mulchaey, J.S. & Regan, M.W. 2006, *ApJ*, 636, 654

Ruden, S.P., Glassgold, A.E. & Shu, F.H. 1990, *ApJ*, 361, 546

Ruiz, J.R., Crenshaw, D.M., Kraemer, S.B., Bower, G.A., Gull, T.R., Hutchings, J.B., Kaiser, M.E. & Weistropp, D., 2001, *AJ*, 122, 2961

Ruiz, J.R., Crenshaw, D.M., Kraemer, S.B., Bower, G.A., Gull, T.R., Hutchings, J.B., Kaiser, M.E., Weistropp, D. 2005, *AJ*, 129, 73

Safier, P.N. 1993, *ApJ*, 408, 115

Schulz, H. 1990, *AJ*, 99, 1442

Shang, H., Glassgold, A.E., Shu, F.H. & Lizano, S. 2002, *ApJ*, 564, 853

Shields, G.A. 1977, *Ap. Letters*, 18, 119
Shlosman, I., Vitello, P.A. & Shaviv, G. 1985, *ApJ*, 294, 96
Smith, M.D. 1984, *MNRAS*, 209, 913
Steffen, W., Gómez, J.L., Williams, R.J.R., Raga, A.C. & Pedlar, A. 1997,
MNRAS, 286, 1032
Wilson, D.B. 1982, *MNRAS*, 200, 881

Winge, C., Axon, D.J., Macchetto, F.D., Capetti, A. & Marconi, A. 1999, *ApJ*,
519, 134
Woods, D.T., Klein, R.I., Castor, J.I., McKee, C.F., Bell, J.B. 1996, *ApJ*, 461,
767